# Paper IV



T. Makkonen, S. Kondratiev, V. P. Plessky, T. Thorvaldsson, J. Koskela, J. V. Knuuttila, and M. M. Salomaa, “Surface acoustic wave impedance element ISM duplexer: modeling and optical analysis”, IEEE Transactions on Ultrasonics, Ferroelectrics, and Frequency Control, Vol. 48, No. 3, pp. 652–665, May 2001.

# Surface Acoustic Wave Impedance Element ISM Duplexer: Modeling and Optical Analysis

Tapani Makkonen, *Member, IEEE*, Serguei Kondratiev, *Member, IEEE*, Victor P. Plessky, *Member, IEEE*, Thor Thorvaldsson, *Member, IEEE*, Julius Koskela, *Member, IEEE*, Jouni V. Knuuttila, and Martti M. Salomaa, *Member, IEEE*

***Abstract*—Surface acoustic wave (SAW) impedance element antenna duplexers provide compact, high performance, front-end components apt for industrial fabrication. We describe investigations on the design and modeling of a compact ISM antenna duplexer fabricated on a 36° YX-cut $LiTaO_3$ substrate based on SAW impedance elements. In particular, we have performed 3-D modeling of the inductive and capacitive electromagnetic couplings caused by the package parasitics for the duplexer. The use of a 1:3 IDT structure for the reduction of the passband width is discussed. The frequency response of the duplexer is predicted with the help of circuit simulation; the modeling is refined by optimization of the model parameters to improve the fit between the measured and simulated responses. We also report scanning optical imaging of the acoustic field within the resonator structures with the help of laser interferometry; this provides insight into the loss mechanisms beyond that attainable in mere electric measurements.**

## I. Introduction

The power handling capability realizable with SAW devices employing ladder structures of SAW resonators (impedance element filters, IEF) has reached a level sufficient for important commercial applications, such as portable phone antenna duplexers [1]–[3]. Because of the good electrical performance, small size, and low cost enabled by SAW technology, it presents a competitive alternative to the more traditional helix and ceramic technologies commonly used for duplexers. As the power requirements defined by system specifications are simultaneously expected to become less stringent, SAW duplexers are a promising alternative for front-end applications in wireless communication systems, also providing cost savings at the system level through simplified matching and manufacturing as well as via reduced board space and component count.

We aim to develop a modeling technique capable of predicting the major aspects of duplexer behavior, including parasitic effects. The procedure is not limited to SAW IEF filters, although we employ it in the modeling of SAW duplexers, which presents the additional challenge of enclosing two filters within a single package. The comprehensive approach presented in this paper for duplexer development includes the optimization of the device design on the chip with advanced modeling strategies, the consideration of package parasitics on the duplexer behavior with special attention devoted to the numerical computation of the parasitic electromagnetic couplings, as well as sophisticated optical measurement techniques for imaging SAW fields. Laser-interferometric imaging of the duplexer provides further insight into features of the device behavior in the passbands, which are not accounted for by the simulations.

## II. Duplexer Function

In analog or digital mobile phone systems, the communication between the base station and the phone occurs at two different frequencies. The signal is transmitted from the phone to the base station within the transmission channel (Tx) with the center frequency $f_T$ and from a base station to the phone within the receiver channel (Rx) with the center frequency $f_R$ (see Fig. 11 for a typical duplexer response). The duplexer component is used to separate or isolate the transmitter and receiver channels, such that a signal may simultaneously be transmitted and received. The duplexer is a three-port device, i.e., the receiver output and the transmitter input ports plus the third port connected to the antenna. Fig. 1 is a block diagram of a modern cellular phone transceiver utilizing SAW components both in the front-end and IF sections. The duplexer encompasses two bandpass filters with the center frequencies $f_T$ and $f_R$, respectively, connected in parallel to the common antenna port. In the case of a SAW duplexer, the two filters may be implemented either fabricating each on a separate chip and packaging them inside a common enclosure or integrating both filters on the same chip. The

Manuscript received July 2, 1999; accepted October 16, 2000. This work is supported by Micronas Semiconductor SA, Micronas Oy (Espoo, Finland), the NOKIA Group, TEKES (Technology Development Centre, Finland), and the Graduate School in Technical Physics.

T. Makkonen, J. V. Knuuttila, and M. M. Salomaa are with the Materials Physics Laboratory, Helsinki University of Technology, FIN-02015 HUT, Finland (e-mail: tapani@focus.hut.fi).

S. Kondratiev is with Temex SAW, CH-2000 Neuchâtel, Switzerland.

V. P. Plessky is with Thales Microsonics, SAW Design Bureau, CH-2000 Neuchâtel, Switzerland.

T. Thorvaldsson is with Thoronics GmbH, CH-2022 Bevaix, Switzerland.

J. Koskela is with Nokia Research Center, FIN-00045 Nokia Group, Finland.

duplexer considered in this paper is of the latter type, allowing a smaller package to be employed and a simpler bonding between the chip and the package to be applied. Because the two filters are in one package, there is more flexibility to improve the performance of a SAW duplexer. Furthermore, the filter interaction (the two channels) may be used to an advantage. Finally, sensitivity caused by parasitics in the application environment is reduced.

Because of the introduction of new wireless standards requiring higher data transmission capability and also because of the increasing number of subscribers for the already established standards, an efficient utilization of the available frequency bands is of paramount importance. The frequency crowding necessitates a high selectivity for the passband filters to accommodate more channels and to avoid the interference of adjacent channels. Although performance specifications are different for the analog and digital systems, many common requirements can be stated. At the transmission frequency $f_T$, both filters need to tolerate the applied power levels, although the power tolerance of the Tx filter is nearly always the limiting factor because the frequency $f_T$ is in the stopband of the Rx filter. However, depending on the channel separation and the stopband suppression level of the Rx filter, the power tolerance of the Rx filter may also become relevant. The duplexer also needs to provide sufficient attenuation at certain critical frequencies. In the transmission channel, an adequate suppression of the noise generated by high power amplifiers on the harmonic bands is required. In the receiver channel, a high attenuation of the image frequency band is important. Furthermore, a sufficiently high attenuation in the frequency bands of the mutual channels has to be attained. Through maximizing the rejection level between the Rx and antenna ports within the Tx band, the interference of the Tx channel within the Rx channel is minimized.

Low insertion losses are essential for Tx, to reduce power consumption, thus extending the operation time possible with single charging of the battery, and for Rx, to increase the sensitivity, thus allowing a more reliable connection. The duplexer considered here is designed for a 50-Ω environment. Hence, the minimum insertion loss (IL) is obtained with a 50-Ω impedance in the antenna port in the passbands for matched operation. In the passband of one channel, the input is also loaded by the mutual channel, which needs to have as high an impedance as possible (close to an open circuit) to avoid any additional losses.

## III. SAW Technology

SAW technology provides filter solutions with lightweight and mechanically robust structure. SAW components are mature for industrial mass production because they can be fabricated in large quantities at competitive prices, employing the well-known photolithographic techniques commonly applied in the IC industry. Comparatively few process steps are needed. Only a single metallization layer (usually aluminum) is fabricated on top of a piezoelectric substrate. However, high quality of the thin electrode fingers (shape, uniformity) in the IDT is necessary. Consequently, the fabrication process has to be controlled with high precision.

The one-port SAW resonators in IEF are connected according to one of several possible schemes, such as the ladder connection shown in Fig. 2. The SAW resonators may be regarded as frequency-dependent impedances (impedance elements) used to synthesize the filter response—thus the name IEF. The operation principle is illustrated in Fig. 2. The (series) resonance of the series resonator roughly coincides with the antiresonance (parallel resonance) of the shunt resonator. At the frequencies of the deep notches on both sides of the passband, the impedance of the series resonator is much larger than that of the parallel resonator; at the notch with lower frequency, this is due to the resonance of the parallel elements, and, at the notch with higher frequency, this is due to the antiresonance of the series elements. Because the voltage drop is divided between the resonators in approximately the ratio of their impedances, the parallel resonator at the notch frequencies is effectively shunted. At the center frequency of the passband, the situation is reversed, and the parallel resonator is effectively open-circuited; the low impedance of the series resonator causes only low losses as the current flows through it to the load.

Modern SAW filters operating in the 1-GHz frequency range are increasingly based on the impedance-element concept. This is due to the several benefits that the impedance-element technology provides, including a low insertion loss, enhanced power-handling capability [5], steep skirts for frequency selectivity, and high close-in rejection. The sharp cut-off frequency characteristics are especially important for duplexers because the transmitter and receiver frequency bands are next to each other. Increasing the number of resonators and connecting them appropriately, the energy can be divided among several resonators; therefore, the energy is spatially spread over a larger area for increased power tolerance. However, this introduces a compromise for the device size. The SAW resonators contain long IDTs with possibly short reflectors at the ends to form the resonator cavity. There are many finger electrodes in parallel, thus resulting in a low resistance at the resonance of the series resonator, which is essential for attaining a low IL.

The suppression level is determined by the ratio of the static capacitances for the series and parallel resonators and the number of sections. Consequently, for high stopband suppression, either an increased capacitance ratio or more sections are needed. This leads to an increase of the IL in the desired passband. The width of the passband of the IEF is proportional to the frequency difference between the antiresonance and the resonance and depends on the capacitance ratio, the number of sections, the type of configuration, and matching.

The IEF are commonly fabricated on high coupling coefficient materials, which usually possess large temperature coefficients in comparison with quartz. The temper-

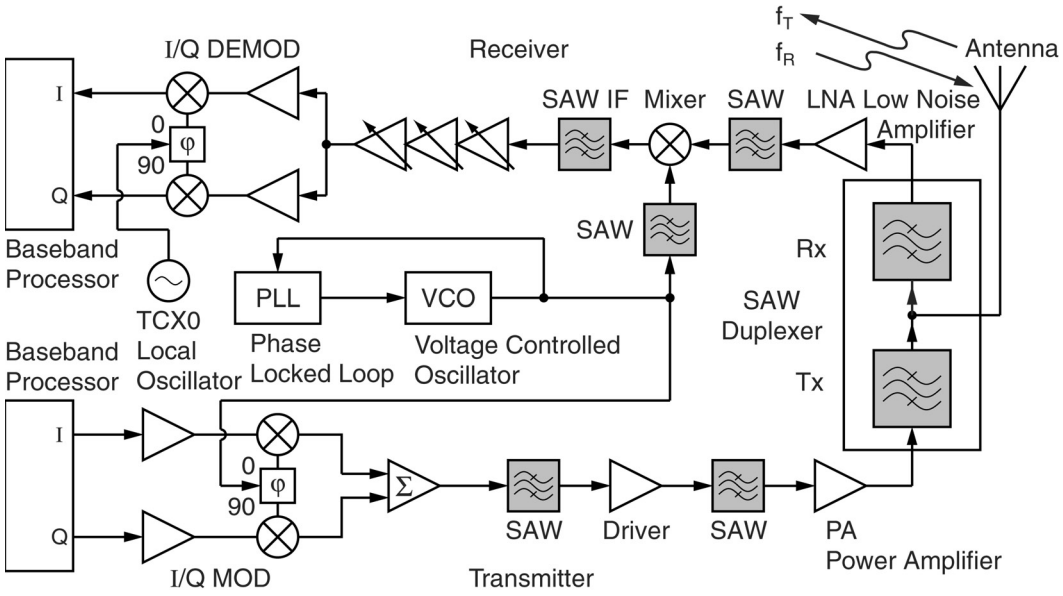


Fig. 1. Block diagram of the RF section in a modern digital cellular phone (adapted from Ref. [4]).

ature coefficient for 36° $LiTaO_3$ is about 30 ppm/°C and 70 ppm/°C for 64°-$LiNbO_3$. The substrate material and its cut are selected according to the application. For example, narrowband IEF of bandwidth 0.005 to 0.5% can be realized on quartz. But, for wideband filters on quartz, the electromechanical coupling is not sufficient. For an ISM duplexer, e.g., we need strong coupling materials, such as $LiTaO_3$.

SAW components are quite sensitive to the shape and quality of the electrodes and any surface contamination (a feature that is utilized to an advantage in sensor applications [6]). To protect the SAW chip from contamination, humidity, and oxidation, it is enclosed in a hermetically sealed package with an inert atmosphere—usually dried nitrogen. For the same reason, it is difficult to introduce a passivation layer over the SAW chip, thereby complicating its integration into a single chip with active RF components.

Recently, it has been demonstrated that SAW technology itself presents no fundamental physical limitations for its extension into the 5-GHz [7]–[9] and 10-GHz [10] frequency ranges. However, the patterning of high frequency prototypes has been accomplished with electron-beam lithography, which is not yet applicable for profitable mass production.

In the following, we consider a SAW IEF ladder duplexer for the ISM band, focusing on 1) the numerical modeling of the package parasitics to predict their effect on the electrical characteristics of the duplexer and 2) complementing laser interferometric investigations of the acoustic field on the SAW chip to derive information on those aspects of the electrical behavior that cannot be accounted for by the applied modeling techniques.

## IV. SAW Antenna Duplexer for the ISM Band

In the duplexer, both the Rx and Tx IEF are placed on the same chip. The filters are implemented by cascading one-port leaky SAW (LSAW) resonators in the ladder configuration. Each channel includes three series and four shunt resonators. The resonators feature a long IDT and short synchronously placed shorted reflection gratings at both ends. The purpose of the grating is to avoid the insertion loss caused by the propagation of the SAW out of the IDT and, secondly, to improve the frequency response. The use of non-synchronous resonators is, in principle, possible, but it complicates device design. The filters are fabricated on a 36° YX-cut $LiTaO_3$ substrate (LSAW) often used for low-loss filters, although a more optimal cut has been found recently [11]. It has been proposed [3] that the LSAW has a deeper penetration depth within the substrate than the Rayleigh-type SAW, resulting in increased power tolerance.

The chip is enclosed into a 5- × 5- × 1.5-$mm^3$ surface-mount type (SMD) ceramic package. Wire bonding is used for the electrical contacts. To reduce the parasitic effects caused by mutual inductances of the bond wires, symmetric wire-bonding geometry has been pursued. The power tolerance is 1 W. The SAW resonators are modeled with the improved COM model [12]–[15].

For $LiTaO_3$, the piezoelectric coupling coefficient is too high, which results in too wide bandwidths (1.5 to 5%) for ISM applications in structures using a "single" finger configuration. To obtain a narrower passband width (0.5 to 1%), a 1:3 finger structure is utilized [16].

### *A. 1:3 Finger Structure*

In the "normal" 1:1 configuration, the fingers are alternately connected to the two busbars [see Fig. 2(a)].

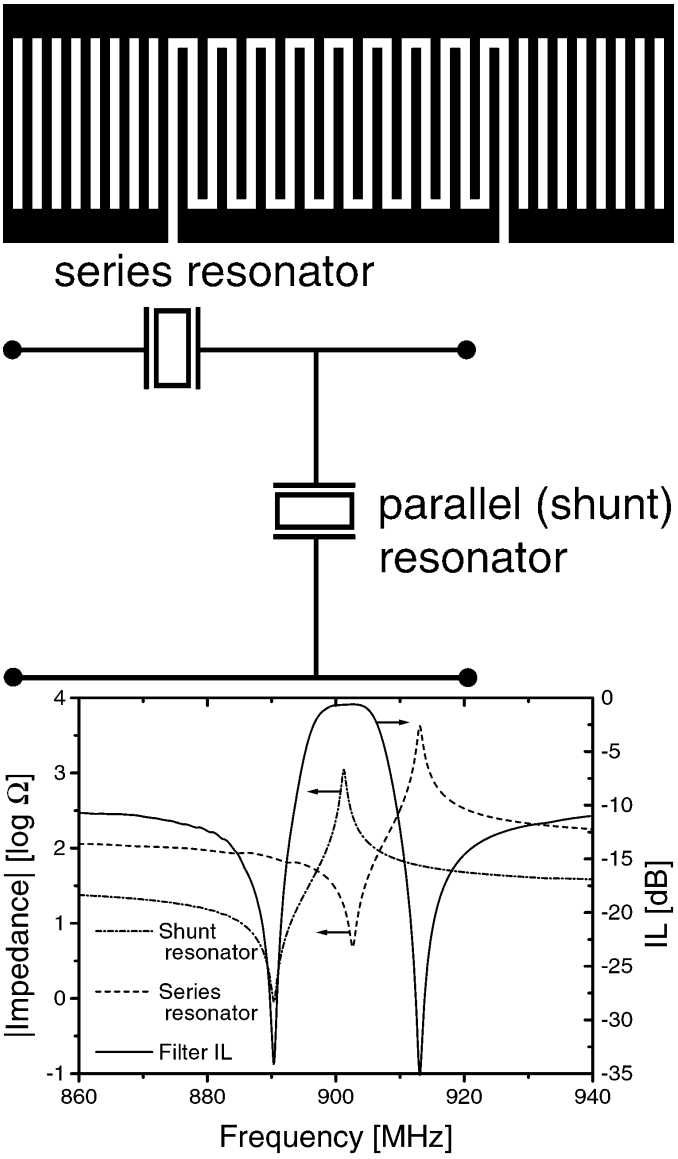


Fig. 2. a) Long IDT track with high internal reflections and reflector gratings at both ends to trap acoustic energy into the resonator, b) basic section for ladder IEF filters, and c) resonance of the series resonator coincides with the antiresonance (parallel resonance) of the shunt resonator.

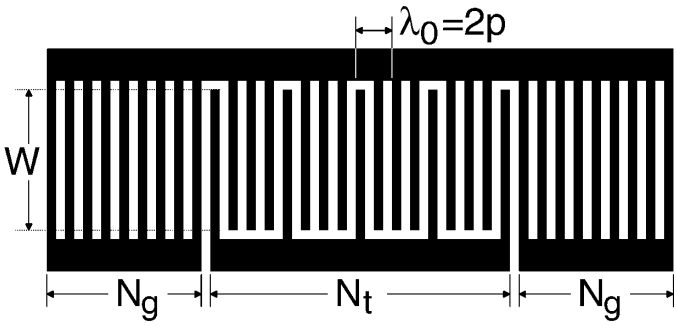


Fig. 3. IDT with 1:3 electrode configuration.

In the 1:3 configuration, every active finger in the IDT—connected to the first busbar—is followed by three fingers connected to the second busbar, as shown in Fig. 3. In this fashion, the coupling efficiency $k_{\text{eff}}$ is approximately halved. Typical IDT parameters for a parallel resonator in the duplexer are number of fingers in the transducer ($N_t = 580$), number of fingers in the reflector gratings ($N_g = 40$), periodicity ($p = 2.25$ $\mu$m), aperture ($W = 60$ $\mu$m), and ratio of the thickness of the metallization layer to the SAW wavelength (5%). In Fig. 4, the electrical conductances measured on wafer with test resonators for the 1:1 finger structure and the 1:3 finger structure are presented. The figures also show the theoretical conductances computed with the coupling-of-modes (COM) model modified to include an additional conductance and attenuation because of the observed acoustic leakage on stopband frequencies and bulk-acoustic wave (BAW) radiation for high frequencies [15]. For the SAW filter synthesis, the COM parameters are extracted from test resonator measurements by a fitting procedure. It is noted, however, that the COM coupling parameter used to model the IDTs in actual devices are different (up to 25%) from those extracted from the test resonator measurements. This is partially due to the fact that the additional metallization outside the IDTs in the actual devices introduces an additional series inductance that is not present in the test resonators. This requires the COM parameters to be accordingly modified for accurate modeling. Discussion over the general behavior of COM parameters can be found [17].

For the 1:3 structure, there are resonance peaks in the filter response also at approximately $f_0/2$, $3f_0/2$, $2f_0$, etc., where $f_0$ is the center frequency of the passband (Fig. 5). Because of dispersion, the subharmonic responses do not occur exactly at $f_0/2$ and $3f_0/2$, which is critical in many cases, to comply with the filter specifications. Because of the increased bulk wave radiation and scattering effects above the frequency $f_0/2$, the losses increase ($\propto f$). At the frequency $f_0$, this serves to increase the IL by approximately 1 to 1.5 dB. In addition to the typical behavior of a decreasing suppression level with increasing frequency (because of the electrical feedthrough) seen in Fig. 5, a trap around the frequency 1.5 GHz is present. It may be formed because of a resonance caused by package parasitics, i.e., the package pin and IDT capacitances, and the bond wire and common package ground inductances [18], [19]. In this case, the trap could be moved to the passband frequencies through redesigning the package layout, thus improving the close-in suppression level.

In Fig. 4, it is seen that, at frequencies immediately above the series resonance, an increased conductance occurs that is not accounted for by the COM model applied (gray regions in Fig. 4). The deviation from theory is more pronounced for the 1:3 IDT structure than for the 1:1 structure, indicating higher relative losses in the former configuration. This effect appears to depend somewhat on the quality and the shape factor of the electrodes, the metallization ratio, and the center frequency of the resonator. It is also relatively stronger for narrower apertures, and it weakens with decreasing metallization ratio. Because the

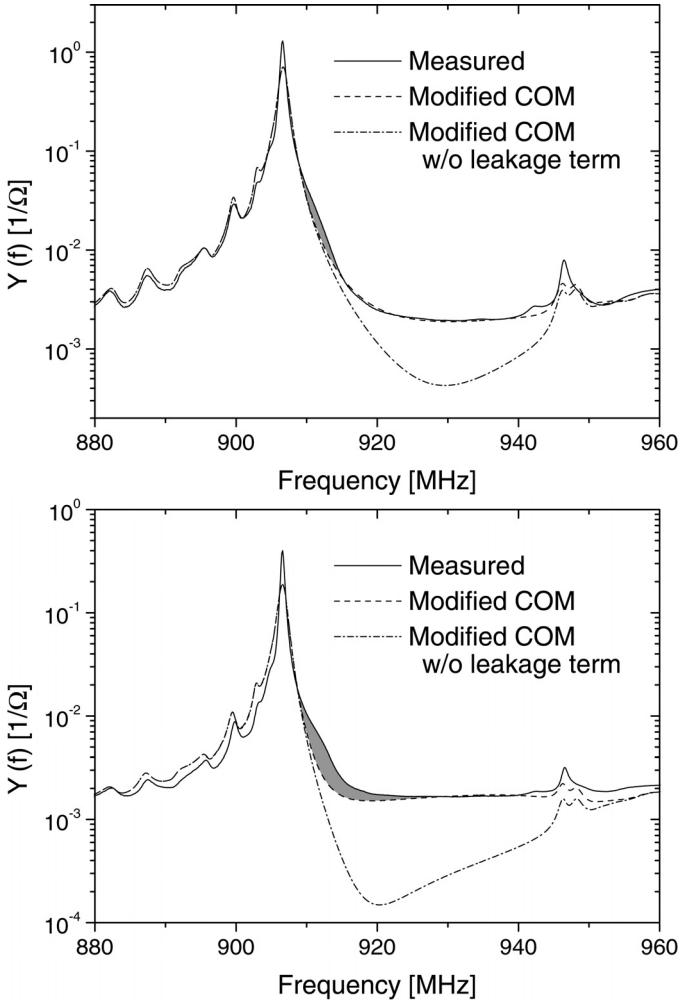


Fig. 4. Measured and fitted conductances of a test structure with a) 1:1 and b) 1:3 electrode configuration on 36° YX $LiTaO_3$ substrate. For discussion of the increased conductance (shaded regions), see Section VII.

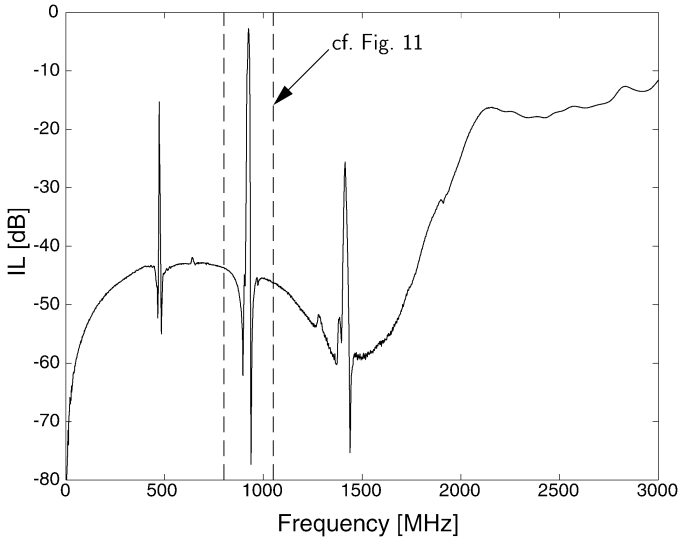


Fig. 5. Measured wideband frequency response of the duplexer (Tx channel) showing the subharmonic and superharmonic resonances. See the text for a discussion of the trap in the response occurring around the frequency 1.5 GHz.

electrical measurements alone cannot give further insight into the underlying acoustic loss mechanisms, we have also carried out laser interferometric measurements to study the acoustic field distribution within the resonators of the duplexer [20], [21]. We discuss this topic in detail in Section VII.

The effective piezoelectric coupling coefficient $k_{\text{eff}}$ can also be reduced through the introduction of a sublayer of amorphous $SiO_2$ between the IDT and the $LiTaO_3$ substrate. By varying the sublayer thickness, the penetration depth of the electric field into the $LiTaO_3$ substrate can be controlled, and, consequently, the $k_{\text{eff}}$ can be reduced. A possible source of complications is the sensitivity of the coupling coefficient to the layer thickness [22], [23]. Therefore, the 1:3 structure is used in the duplexer considered here for the reduction of the passband width.

## V. Parasitics Modeling

Because of the high frequencies employed, the electromagnetic couplings in the SAW package may considerably affect the measured electrical characteristics of the device, in comparison with those measured for an unpackaged device. Usually, the parasitics deteriorate the device performance, but, in some cases, the packaging effects can even be used to improve the performance [18]. If the parasitic electromagnetic couplings can be predicted reliably and taken into account already in the design phase, the specifications can be met more precisely, and, thus, the number of expensive test cycles may be reduced. We aim to predict the frequency response of the packaged device starting from the basic geometry and the appropriate materials parameters of the package. Estimates are numerically computed for the self and mutual inductances of the bond wires as well as for the self and coupling capacitances of the package pins. The inductive couplings between the bond wires generate parasitic effects in the stopband [24], whereas capacitive couplings give rise to a decreased suppression level on the stopband as well as an increased ripple in the passband. The parasitic couplings may also cause a widening of the transition band and a decreased close-in suppression. To avoid this performance degradation requires careful design of the package geometry.

The frequency response of the duplexer is predicted by carrying out a circuit simulation with an equivalent circuit model, including the parasitic lumped elements. The equivalent circuit acts as a bridge between the SAW chip and the printed circuit board (PCB). Here, we compute values for the parasitic elements based only on the package geometry and the materials parameters. Because there exists an uncertainty with respect to the bond wire geometry and the package metallizations caused by manufacturing tolerances, an optimization is utilized to refine the model parameters to fit the measured and simulated frequency responses.

### *A. Modeling Capacitive Parasitics*

For a set of $N$ ideal conductors, there prevails a linear relationship between the charges and the potentials of the conductors, expressed in matrix form as $q = Cv$, where $q$ is the vector of conductor charges, $v$ is the vector of conductor potentials, and $C$ is the capacitance matrix:

$$C = \begin{pmatrix} c_{11} & c_{12} & \dots & c_{1N} \\ c_{21} & c_{22} & \dots & c_{2N} \\ \vdots & \vdots & \ddots & \vdots \\ c_{N1} & c_{N2} & \dots & c_{NN} \end{pmatrix}. \tag{1}$$

Connecting the conductor $i$ ($i = 1, 2, \dots, N$) to the potential 1 V and grounding all of the remaining conductors, a positive charge equal to the diagonal element $c_{ii}$ of the capacitance matrix is induced to the conductor $i$ and a negative charge equal to $c_{ij} = c_{ji}$ is induced to the conductor $j$ ($i \neq j$). Hence, the off-diagonal elements of the capacitance matrix are negative.

Estimates for the capacitive parasitics are computed using the program FastCap [25], [26], which is capable of numerically evaluating the capacitance matrix for 3-D geometries of ideal conductors embedded in linear, isotropic, and piecewise homogeneous dielectrics. It is based on the boundary element method (BEM) under the static approximation, i.e., it is assumed that the potential on each conductor can be taken constant to a fair approximation. This assumption is valid if the signal path length is smaller than one-tenth of the wavelength [27], which approximately holds for the duplexer package modeled. For the capacitance extraction, the integral equation relating the electric potential and the surface charge is discretized by subdividing the conductor surfaces and dielectric boundaries into small surface elements or tiles. The charge density on each element is assumed constant. The iterative solution of the resulting dense system of linear equations for the unknown element charges is accelerated by using multipole and local expansions in the evaluation of the matrix-vector products involved.

*1. Model and Computed Capacitances for the Duplexer Package:* The duplexer package considered consists of three sub-layers, which makes the task of modeling the package geometry quite demanding. The model of the package for the capacitance extraction is displayed in Fig. 6 (with the lid removed). All of the three sub-layers of the package (also the metallizations on the bottom face of the package and the lid) are included into the model, and they all contribute to the computed capacitance matrix. In the modeling, we have neglected the capacitive couplings between the package pins and the pads on the SAW chip. A possible complication with the computational method is that the charge density is approximated with a pulse function (i.e., constant charge density on the surface elements). The pulse function cannot exactly model the actual strongly varying charge density on the conductor edge regions; consequently, there results a corresponding loss of accuracy.

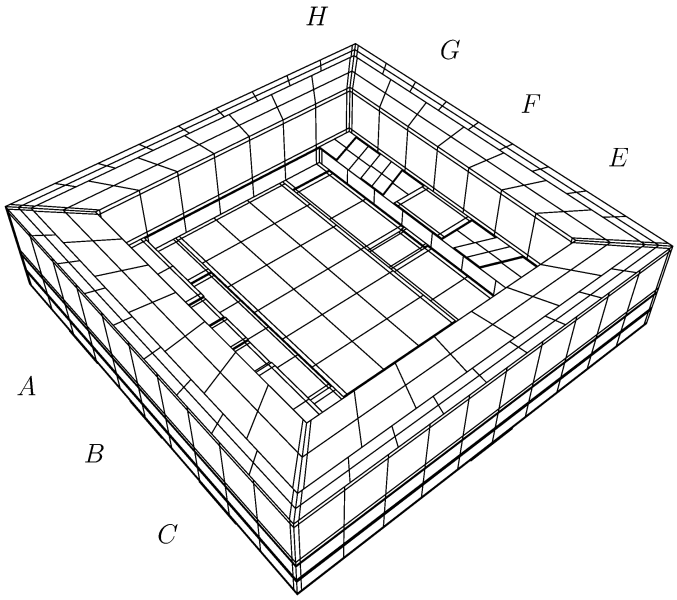


Fig. 6. Discretized geometry of the duplexer package model for the capacitance extraction. For clarity, the grounded lid of the package is not shown. The discretization illustrated is also coarser than those used in the actual computations.

TABLE I
NUMERICALLY COMPUTED CAPACITANCE MATRIX (fF) FOR THE PINS OF THE DUPLEXER PACKAGE.

| | Ground | Antenna | Rx | Tx |
|---|---|---|---|---|
| Ground | 1450 | −339.6 | −450.6 | −410.0 |
| Antenna | | 346.7 | −0.1473 | −0.1553 |
| Rx | | | 457.8 | −0.9244 |
| Tx | | | | 418.0 |

The computed values (in femtoFarads, fF) for the self and coupling capacitances (for a model with 41 090 surface elements) are presented in Table I. Under charge conservation, the sum of the elements in each row or column would equal zero. However, upon connecting a conductor $i$ to the potential of 1 V and grounding the others, a portion of the positive charge on the conductor $i$ is induced to support the electric field lines terminating to zero potential at infinity (the stray field). The self-partial capacitance $C_{i0}$ in the equivalent circuit for the conductors, associated with the stray field of conductor $i = 1, 2, \dots, N$ is related to the elements of the capacitance matrix through [28]

$$C_{i0} = \sum_{k=1}^{N} c_{ik} = \sum_{k=1}^{N} c_{ki}, \quad i = 1, 2, \dots, N; \tag{2}$$

the mutual partial capacitance $C_{ij}$, expressing the strength of the capacitive coupling between conductors $i$ and $j$, is

$$C_{ij} = -c_{ij}, \quad i \neq j; \quad i, j = 1, 2, \dots, N. \tag{3}$$

Taking the ground metallization to reside at zero potential, e.g., the Rx pin to ground capacitance in the equivalent

circuit of the package may be derived as $C_{30}+C_{13} = c_{23}+c_{33}+c_{34} = 456.7$ fF. Also, the direct bridge capacitance $C_{23}$ from the input to the output in the Rx channel (from antenna pin to the Rx pin) equals $C_{23} = -c_{23} \approx 0.15$ fF.

The discretization error is estimated via computing the capacitances employing two different discretizations. The finer discretization included 14.7% more surface elements (41 090) than the coarser one (35 798), the difference in the off-diagonal elements being less than 3%. That for the diagonal elements is approximately 0.5%, which is better than the 1% accuracy of the iterative solver. The computation for the more refined model required 876 Mb memory and 15 min 35 s CPU time on a Compaq AlphaServer 8400 computer.

### *B. Modeling Inductive Parasitics*

The program FastHenry [29] is utilized in the numerical computation of the frequency-dependent bond wire self and mutual inductances in the presence of two ground planes. The program assumes linear and isotropic conductors and magnetic media, and it is based on the discretization of the integral equation

$$\frac{\mathbf{J}(\mathbf{r})}{\sigma} + \frac{j\omega\mu}{4\pi}\int_{V_c}\frac{\mathbf{J}(\mathbf{r}')}{|\mathbf{r}-\mathbf{r}'|}dv' = -\nabla\Phi(\mathbf{r}), \qquad (4)$$

relating the current density $\mathbf{J}$ and the scalar potential $\Phi$. In (4), $\sigma$ is the conductivity, $\omega$ is the angular frequency, and $\mu$ is the permeability. The discretization is accomplished through dividing the conductor volumes into small elements or filaments. The unknown current density is expressed as the sum of the uniform currents flowing in each volume element and the method of moments is applied to obtain a (dense) linear system of equations. The equations are reformulated using the mesh-analysis approach to render the system suitable for an iterative solution. The solution procedure is equivalent to that used in the FastCap program.

*1. Skin and Proximity Effects:* At high frequencies, the current tends to concentrate onto the outer surface of a conductor. Because of this so-called skin effect [30], the self and mutual inductances and the resistances become frequency dependent. The proximity effect [31], i.e., the presence of other nearby current-carrying wires, also modifies the current distribution in the wire. A test geometry of two adjacent and parallel bond wires, depicted in Fig. 7, is used to examine the skin and proximity effects. The discretization error is also investigated as a function of the number of the volume elements to find a compromise between computing time and the numerical accuracy.

The bond wires are modeled to feature a parabolic shape; they are discretized into a chain of straight segments with rectangular cross-sections to approximate the actual geometry. To properly model the uneven current distribution caused by the skin effect, the segments are further subdivided into parallel filaments assuming a uniform current. At high frequencies, most of the current flows in the vicinity of the surface. FastHenry takes this into account by allowing a nonuniform discretization with a smaller cross-section for the filaments near the surface of the conductor and, correspondingly, a larger one toward the interior regions.

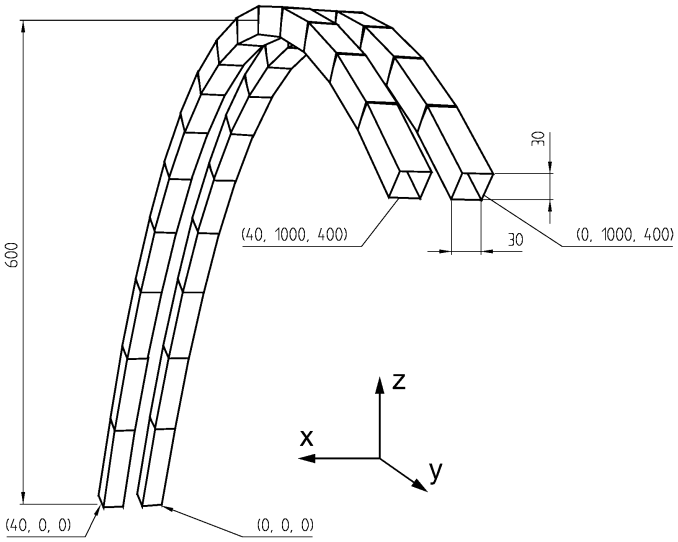


Fig. 7. Geometry of two bond wires in parallel planes used in the investigation of the skin and proximity effects. Lengths are in micrometers.

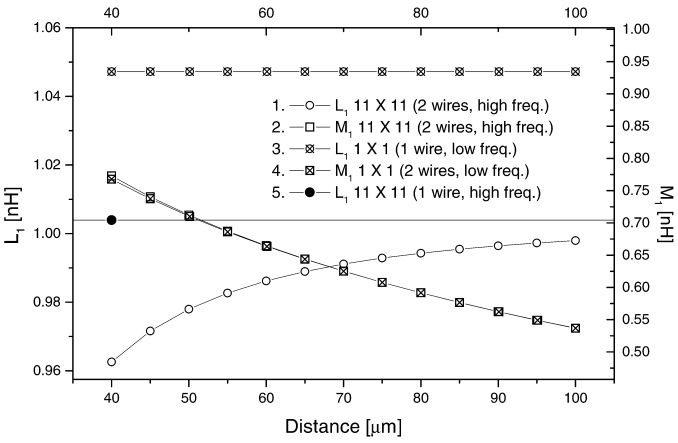


Fig. 8. Computed inductances for the geometry in Fig. 7 at 1-GHz frequency as a function of the distance between the midpoints of the bond wires [$\sigma = 37.7 \times 10^6$ $(\Omega\text{m})^{-1}$].

Fig. 8 depicts the skin effect that lowers the self inductance, as seen in the difference between the computed self inductances $L_1$ for one wire with the $1\times1$ and $11\times11$ discretizations. Only a uniform current distribution can be modeled with the $1\times1$ discretization, and, hence, this case yields the self inductance at low frequencies. The proximity effect changes the self-inductance as a function of the distance between the midpoints of the bond wires. This is seen as the difference between the two wires, $11\times11$ and 1 wire, $11\times11$ discretizations. The mutual inductance $M_1$ depends only weakly on the current distribution in the wires, as indicated by the nearly equal mutual inductances for the two different discretizations.

TABLE II
COMPUTED SELF INDUCTANCES AND RESISTANCES OF ONE BOND WIRE FOR DIFFERENT DISCRETIZATIONS AT 1-GHz FREQUENCY [$\sigma = 37.7 \times 10^6$ $(\Omega\text{M})^{-1}$]. SELF INDUCTANCES ARE IN nH, AND RESISTANCES ARE IN $\Omega$.

| # of segs. | Filaments/ segment | Self inductance | Resistance |
|---|---|---|---|
| 10 | $11 \times 11$ | 1.00 | 0.147 |
| 10 | $7 \times 7$ | 1.00 | 0.146 |
| 10 | $5 \times 5$ | 1.01 | 0.145 |
| 5 | $7 \times 7$ | 0.997 | 0.144 |
| 5 | $5 \times 5$ | 0.998 | 0.143 |
| Straight wire | | | |
| 10 | $11 \times 11$ | 1.10 | 0.147 |

To accurately model the skin effect as a function of frequency with a reasonable number of filaments and moderate CPU times, the discretization is performed adaptively. For coarse discretizations, the ratio between the widths of the adjacent filaments, $k$, is computed such that the width of the outermost filaments equals the skin depth. Table II summarizes the computed self inductances (in nanoHenrys, nH) and resistances (in Ohms, $\Omega$) as functions of the discretization. The geometry included only one of the bond wires in Fig. 7. Comparing the self inductances for the five segments, $5 \times 5$ discretization, and the finest discretization, their difference is below 1%. This lies within the tolerance because the error resulting from the uncertainty in the geometry of the bond wires exceeds this. However, the computed resistance depends more strongly on the number of filaments and also on the value of $k$. An estimate for the alternating current resistance of a circular wire is computed using a formula from [30]:

$$\frac{R}{R_0} = \frac{\pi r^2}{\pi(2r-d)d} \tag{5}$$

where $R$ is the alternating current resistance, $R_0$ is the direct current resistance, $r$ is the radius of the wire, and $d = (\pi f \mu \sigma)^{-1/2}$ is the skin depth at frequency $f$. Substituting numerical values, one finds that, at the frequency 1 GHz, the resistance of a circular Al wire with a radius of 16.9 $\mu$m is already 3.5 times the DC resistance. For a straight 1.34 mm long wire, this yields a resistance of 0.140 $\Omega$. For the AC resistance $R$ of a rectangular wire [32],

$$\frac{R}{R_0} = \frac{h(b/a)}{\pi}\sqrt{\mu f \sigma A}. \tag{6}$$

where $R_0$ is the DC resistance, $A$ is the cross-sectional area of the wire, and

$$h(b/a) = \frac{2}{\sqrt{\pi}}\sqrt{E - \kappa_1^2 F}\sqrt{E' - \kappa^2 F'}(F + F'). \tag{7}$$

In (7), $E$ and $F$ are complete elliptic integrals of the first and second kinds to modulus $\kappa$, respectively, and $E'$ and $F'$ are those to modulus $\kappa_1 = \sqrt{1-\kappa^2}$. The modulus $\kappa$ for a given ratio of the height and width of the rectangular conductor $b/a$ is solved from the implicit equation

$$\frac{b}{a} = \frac{E'(\kappa) - \kappa^2 F'(\kappa)}{E(\kappa) - \kappa_1^2 F(\kappa)}. \tag{8}$$

For a square cross-section, $h(1) = 1.772$, resulting in the AC resistance $R = 0.145$ $\Omega$ for a square wire with length 1.34 mm. This compares well with the numerically computed values in Table II. One sees that the curvature of the wire does not change the resistance but decreases the self inductance by approximately 10%.

We also investigated the frequency dependence of the self and mutual inductances [33]; it was found that they depend on frequency only weakly (see [27] for measured data on the frequency dependence of the inductance of a package lead). Thus, the inductances are taken as constants in the circuit simulation over the whole frequency range of simulation. In contrast, the computed results indicate that the resistance is strongly frequency dependent around the 1-GHz frequency range of interest where the skin depth is already much less than the diameter of the wire. The bond wire resistance can be compared with that of the Al finger electrodes in the SAW resonators: for an IDT with 300 fingers and an aperture of 15 wavelengths at the frequency 950 MHz, a resistance of 0.03 $\Omega$ is estimated [34]. Nevertheless, the contact resistance caused by the attachment of the bond wire and busbar is dominating, being on the order of 1 $\Omega$.

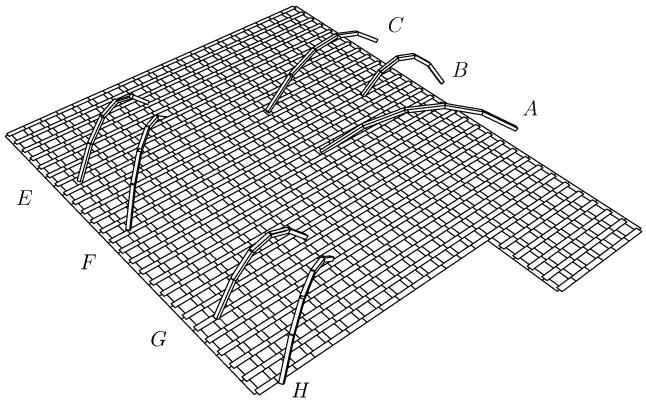


Fig. 9. Discretized geometry of the bond wires and the ground plane under the SAW die in the duplexer. For clarity, the grounded lid over the bond wires is not shown. The segments of the ground plane are also shown narrower than the actual width.

*2. Model and Computed Inductances for the Duplexer Package:* The geometrical model for the bond wires and the lower ground plane in the duplexer is shown in Fig. 9. The bond wires are discretized in five consecutive segments and $5 \times 5$ filaments per segment using the adaptive discretization. The ground plane under the SAW die is discretized with a 2-D grid of $30 \times 20$ segments. The grounded lid of the package contains $30 \times 30$ segments.

The numerically computed self and mutual inductances of the bond wires at the frequency 910 MHz are listed in Table III. The row and column labels correspond to

TABLE III
INDUCTANCE MATRIX (nH) OF THE DUPLEXER BOND WIRES AT 910-MHz FREQUENCY.

| | A | B | C | E | F | G | H |
|---|---|---|---|---|---|---|---|
| A | 1.48 | 0.144 | 0.167 | −0.0453 | −0.0358 | −0.0554 | −0.0400 |
| B | | 0.738 | 0.127 | −0.0216 | −0.0178 | −0.0242 | −0.0198 |
| C | | | 1.39 | −0.0669 | −0.0695 | −0.0527 | −0.0514 |
| E | | | | 0.825 | 0.163 | 0.0502 | 0.0464 |
| F | | | | | 1.01 | 0.0664 | 0.0668 |
| G | | | | | | 0.780 | 0.136 |
| H | | | | | | | 0.896 |

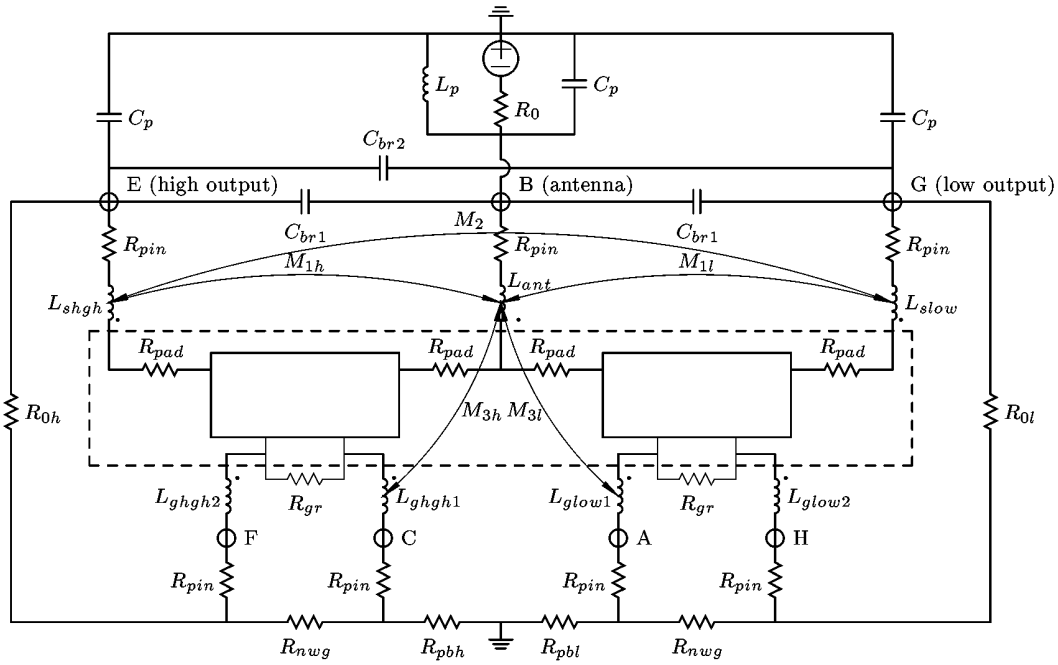


Fig. 10. Equivalent circuit model for the duplexer, including the parasitic lumped elements. Those elements inside the dotted line are on the SAW chip. See Section VI for an explanation of the notation.

those in Fig. 9 and 10. The diagonal elements are the self inductances, and the off-diagonal elements are the mutual inductances, e.g., the element on row B and column G represents the mutual inductance between the bond wires $B$ (antenna) and $G$ (low frequency channel signal). The result is computed for wires with a rectangular cross-section—hence, the values are slightly different for the actual bond wires. The self inductance of the bond wires sometimes produces impedance matching, thus resulting in an improved IL.

The input geometry is discretized using 4245 filaments, the computation requires 34.2 MB memory and the CPU time is 3 min 59 s on a Compaq AlphaServer 8400 computer.

## VI. Equivalent Circuit

The equivalent circuit model of the duplexer is presented in Fig. 10. It can be used to simulate measurements both on wafer and those on the packaged device. Because the transmitter and receiver channels are tightly coupled to each other, it is impossible to treat them independently. For clarity, only five of the mutual inductances are indicated in Fig. 10. The dotted line demarks the chip package boundary. The admittances of the SAW resonators are computed according to the improved COM model [13], [14]. It includes the parasitic electrode resistances. The additional resistances caused by the pads and busbars are denoted with $R_{\mathrm{pad}}$. Ohmic losses in the package pins, bond wires, and contacts are accounted for by the resistors $R_{\mathrm{pin}}$.

The resistance of the connection between the two ground pads is denoted as $R_{\mathrm{gr}}$. This connection is broken when the wafer is cut and the chip is packaged. However, when modeling responses measured directly on wafer, the resistance $R_{\mathrm{gr}}$ must be included. For on-wafer measurements, the two ground pads are also connected through the network analyzer; the resistance of this connection is denoted as $R_{\mathrm{nwg}}$. Moreover, there flows no ground current in the inactive channel; this is mimicked by assigning a large value to the resistor $R_{\mathrm{pb}}$. For measurements on jig

or on PCB, the ground connection is good and $R_{\mathrm{nwg}} = 0$.

The feedthrough capacitances between the input and the two outputs are denoted as $C_{\mathrm{br1}}$; the bridge capacitance between the outputs is $C_{\mathrm{br2}}$. The capacitance $C_{\mathrm{p}}$ is the package pin capacitance to the ground. In the passband of one channel, the input is loaded not only by $R_0$ but also by the other channel, which appears capacitive. To compensate for it, a parallel matching inductor $L_{\mathrm{p}}$ may be used to improve the insertion loss.

### *A. Measurements and Fitting Results*

The circuit simulations were performed both with MATLAB and with the APLAC [35] analog circuit simulator. The simulation with the numerically computed values of the inductive and capacitive couplings given in Tables I and III yields satisfactory results. To improve the agreement between theory and experiment, a fitting procedure of the model parameters is carried out. The theoretical estimates given in Tables I and III are used as the initial values in the optimization.

The measured frequency response and the simulated response obtained with the optimized parasitic component values and COM parameters are plotted in Fig. 11. One observes that the model correctly predicts all features in the stopband, as well as the levels of suppression in the most important regions of mutual passband channels. The effects on the mutual passbands can be mainly attributed to the inductive interactions between the bond wires on different channels.

The quality of the fit is reduced in the passband part of the curves, where the measured data exhibits a notch on the lower edge of the passband, causing a narrowing of the passband and a rounded shape. A similar effect can be seen in the measurement results published by other authors [1], [2], [36]. The phenomenon is frequency dependent and appears weak in the 1:3 test structures with a metallization ratio of 0.5, operating at the frequency 460 MHz. The notch is not due to the parasitic effects of the package but, rather, can be attributed to an acoustic leakage in the shunt resonators. In the electrical measurements, this leakage causes the increased conductance above the series resonance seen in Fig. 4. The acoustic leakage is clearly identified in the laser interferometric measurements presented in the next section. In [36], the filter transmission characteristics at the lower passband edge are improved through using additional matching SAW series resonators between the IEF ladder sections to reduce the impedance mismatch between the sections.

The values of the inductances before and after the optimization differ with a mean square deviation of 50% or more. One reason for the difference is that the fitted parameters are often not orthogonal and have a similar effect on the device performance. We have also omitted many elements, e.g., some of the possible minor mutual inductances and the common ground impedance of the package. Our results indicate that the modeling approach described previously can predict the major characteristics of the measured frequency response. The parasitics modeling provides a means for comparing the performance of the proposed package geometries and bonding schemes with economical computation, prior to the fabrication of costly prototypes.

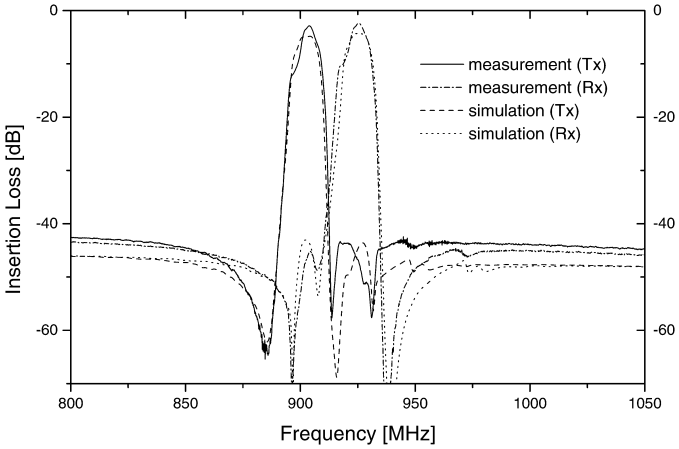


Fig. 11. Experimental and simulated frequency responses. The simulation is carried out with the optimized values for the parasitics. See Fig. 5 for the wideband Tx channel response.

## VII. Optical Analyzing of the SAW Duplexer

### *A. Laser Interferometer*

The optical device used for SAW imaging is a Michelson laser interferometer. A more detailed description of our setup can be found in [37], [38]. The interferometer has been developed for probing modern, high frequency SAW devices operating in the 1-GHz range. Fast automatic computer-controlled focusing and a high precision XY translation system provides 2-D scans with a resolution better than 1 $\mu$m and with measuring speeds up to 50 000 points/h.

At each probing point, the interferometer can detect vibrations normal to the surface. Software controls the stages, performs focusing, and records the measured data at each point. In addition, the intensity of the beam reflected from the SAW chip is recorded at each scanning point, and the values obtained are used for creating a microscope-like image of the area scanned. The setup allows an arbitrary number of scanning points; our largest scans have included over 450 000 points.

### *B. Interferometric Results*

A prototype duplexer with the 1:3 finger structure, featuring a pronounced notch in the passband, was chosen for the laser interferometric analysis. Both the Rx and Tx channels were probed at various frequencies, but, because the results proved equivalent for both channels, only selected scans from the Rx channel are presented here.

In Fig. 12, the IL of the Rx channel is plotted along with arrows indicating the frequencies probed. The measured SAW field at 925 MHz is shown in Fig. 13. The

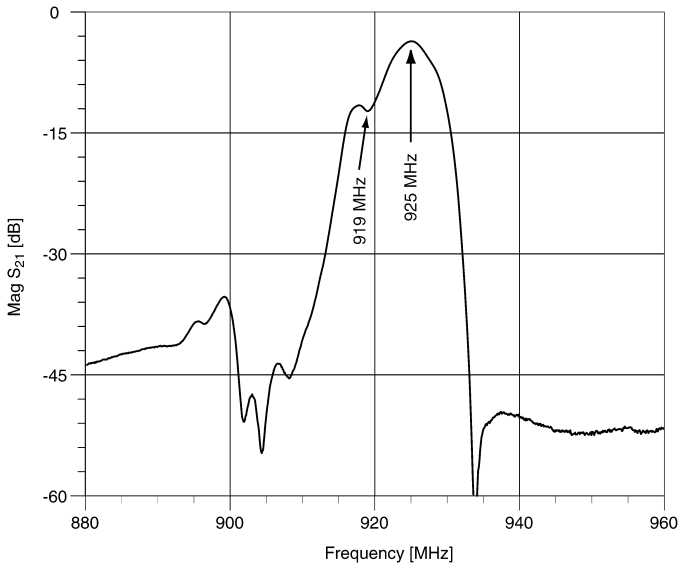


Fig. 12. Frequency response in the Rx channel of the duplexer chosen for the laser interferometric analysis. The frequencies scanned are identified with arrows.

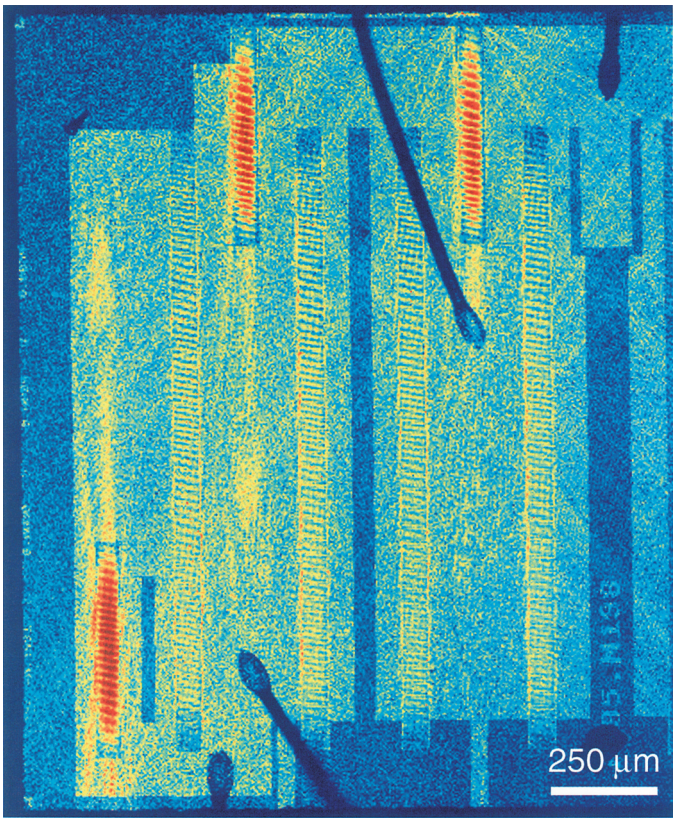


Fig. 13. Acoustic field at 925 MHz, imaged with the scanning laser interferometer. The short and long resonators are series and shunt resonators, respectively. At this frequency, the duplexer operates as designed.

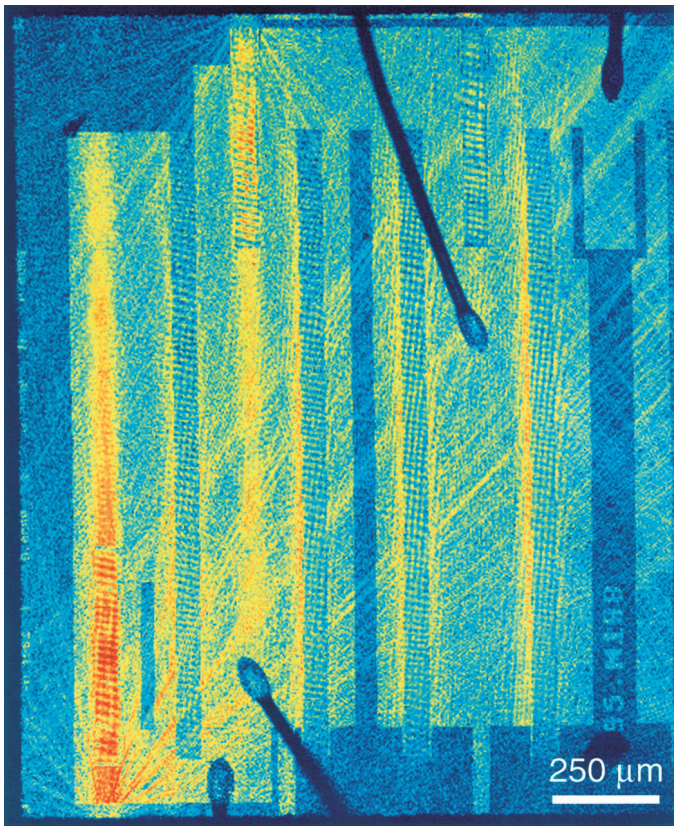


Fig. 14. Acoustic field at 919 MHz, imaged with the scanning laser interferometer. The short and long resonators are series and shunt resonators, respectively. Unwanted acoustic leakage is clearly visible at the left edges of the shunt resonators seen in the middle of the figure.

scanning area is selected to cover the complete Rx section of the duplexer, and it features $420 \times 500$ points. The (frequency-dependent) dynamic range of the scan is better than 40 dB. The periodic, slightly tilted structure on top of the resonators is due to the scanning step. The finite step of 3.85 $\mu$m produces a quantization effect because the standing-wave profile on top of the IDT has a shorter period of $\approx$ 2 $\mu$m. A drawback of the imaging method is that its sensitivity depends on the reflectivity of the surface being probed. This is seen as a discontinuity in the measured field at the edges of the highly reflecting Al metallization and poorly reflecting bare crystal surface. However, part of the difference is due to the fact that, on the metallized surface, the ratio of the vertical component of the particle displacement—detected by the interferometer—to the dominating transversal component is small for the LSAW, and, on crystal surface, it reduces further [39], [40]. The three series resonators show high amplitudes, as expected, because the measuring frequency is set close to the resonance frequency of the series resonators. Acoustic energy is effectively confined within the resonators, although a slight leakage of acoustic energy into the longitudinal direction through the reflectors can be observed. The proper operation of the resonators is predictable because the minimum IL of the duplexer occurs at this frequency.

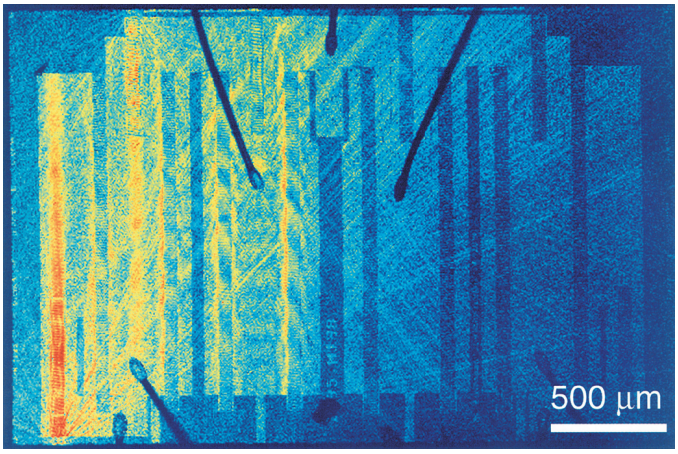


Fig. 15. Acoustic field at 919 MHz. The Rx channel is on the lhs, and the Tx channel is on the rhs.

At the notch frequency of 919 MHz, the series resonators exhibit leakage of acoustic energy into the longitudinal direction through the reflectors (Fig. 14). This acoustic leakage is simulated by the COM model, and it is due to the frequency being below the stopband of the series resonators. What is more important, unprecedented acoustic leakage can be observed in the shunt resonators [41], as is also seen in Fig. 14. The acoustic amplitude is concentrated on the busbar of the shunt resonator, and the wave propagates past the reflector grating, escaping the resonator. This acoustic loss is a manifestation of the crystal anisotropy [42], [43]. It causes the aforementioned increase in the conductance of the resonator seen in Fig. 4 [41] and, consequently, is responsible for the notch detected around the lower passband edge frequencies.

Seen in the lower part of Fig. 14, the SAW beam escaping the series resonators through the reflectors propagates to the crystal edge. Because the crystal edge is rough, the reflected beam is nonuniform but possesses several narrow beams that are scattered to propagate with varying angles away from the edge.

To investigate these beams, a scan covering the complete duplexer was performed and is included in Fig. 15. Although the beams attenuate under propagation, they can still be observed beyond 1 mm away from their points of origin. The bond wires cause the energy of the propagating SAW to diffract into various directions, much like the irregular edge of the crystal, thus effectively blocking the propagating acoustic beam—a phenomenon that could possibly be exploited to prevent unwanted acoustic coupling—or as an absorber.

## VIII. Discussion

A procedure for modeling an impedance element ladder-type SAW antenna duplexer for the ISM system with emphasis on numerical modeling of the inductive and capacitive parasitic couplings in the package is presented along with laser interferometric imaging of the acoustic fields in the SAW resonators. The duplexer considered shows good performance with a minimum IL of 2.5 dB and over 40-dB mutual channel suppression enclosed into a small $5 \times 5 \times 1.5$ mm$^3$ surface-mount type (SMD) package. To reduce the bandwidth, a 1:3 finger structure is used in the IDTs to decrease the coupling coefficient.

In the filter synthesis, the improved coupling-of-modes model is applied in the modeling of the individual one-port LSAW resonators that serve as the building blocks of the impedance element (IE) filters. An equivalent circuit for the duplexer is presented, including the inductive, resistive, and capacitive package-parasitic effects through lumped elements. Estimates for the values of the parasitic lumped elements are given, and the numerical methods used for their computation are shortly described. Modern workstations already have sufficient computational power to effectively carry out the numerical modeling, which allows for a comparison of various package pin and bonding designs with respect to the resulting device performance.

Because of the uncertainty in the package parameters, e.g., bond wire geometry and pin-metallization dimensions, a fitting procedure is carried out to further improve the agreement between the measured and simulated responses. Our modeling allows us to predict the major features of the duplexer behavior, including parasitic effects.

Laser interferometric analysis is used to obtain further insight into those losses not accounted for by the theoretical modeling techniques. The imaging revealed an unexpected asymmetric acoustic leakage in the resonators above the series resonance—which, in further studies, has been confirmed as the source of the electrically observed losses [41].

## Acknowledgments

All of the duplexer samples were designed, manufactured, and tested at Micronas Semiconductor SA (Bevaix, Switzerland). The authors thank Clinton S. Hartmann (Hartmann Research), Christian Lambert (Micronas Semiconductor SA), and Saku Lehtonen (Helsinki University of Technology) for discussions; Pasi Tikka for constructing the jig for the laser-interferometric measurements; and Senior Vice President Yrjö Neuvo (NOKIA Group) for his pertinent interest in our work.

## References

[1] O. Ikata, Y. Satoh, H. Uchishiba, H. Taniguchi, N. Hirasawa, K. Hashimoto, and H. Ohmori, "Development of small antenna duplexer using SAW filters for handheld phones," in *IEEE Ultrason. Symp. Proc.*, pp. 111–114, 1993.

[2] N. Shibahaki, K. Sakiyama, and M. Hikita, "Precise design technique for a SAW-resonator-coupled filter on 36° YX $LiTaO_3$ for use in a GSM SAW duplexer module for satisfying all GSM system specifications," in *IEEE Ultrason. Symp. Proc.*, pp. 19–24, 1996.

[3] C. K. Campbell, *Surface Acoustic Wave Devices for Mobile and Wireless Communications*. San Diego, CA: Academic Press, 1998.

[4] K. Hashimoto, "Surface acoustic wave devices in modern communications systems and their simulation technologies," unpublished.
[5] J.-P. Laine, V. P. Plessky, and M. M. Salomaa, "Investigations on the power tolerance of ladder impedance-element SAW filters," in *IEEE Ultrason. Symp. Proc.*, pp. 15–18, 1996.
[6] E. Benes, M. Gröschl, F. Seifert, and A. Pohl, "Comparison between BAW and SAW sensor principles," *IEEE Trans. Ultrason., Ferroelect., Freq. Contr.*, vol. 45, no. 5, pp. 1314–1330, 1998.
[7] F. Hollerweger, A. Springer, R. Weigel, W. Ruile, R. Thomas, S. Berek, and M. Guglielmi, "Design and performance of a SAW ladder-type filter at 3.15 GHz using SAW mass production technology," in *IEEE MTTS Digest*, vol. 4, pp. 1441–1444, 1999.
[8] H. Odagawa, T. Meguro, and K. Yamanouchi, "5 GHz range low-loss wide band surface acoustic wave filters using electrode thickness difference type unidirectional transducers," *Jpn. J. Appl. Phys., Part 1*, vol. 35, no. 5B, pp. 3028–3031, 1996.
[9] S. Lehtonen, J. Koskela, M. M. Salomaa, V. P. Plessky, M. Honkanen, and J. Turunen, "Surface acoustic wave impedance element filters for 5 GHz," *Appl. Phys. Lett.*, vol. 75, no. 1, pp. 142–144, 1999.
[10] H. Odagawa and K. Yamanouchi, "10 GHz range extremely low-loss surface acoustic wave filter," *Electron. Lett.*, vol. 34, no. 9, pp. 865–866, 1998.
[11] K. Hashimoto, M. Yamaguchi, S. Mineyoshi, O. Kawachi, M. Ueda, G. Endoh, and O. Ikata, "Optimum leaky-SAW cut of $LiTaO_3$ for minimised insertion loss devices," in *IEEE Ultrason. Symp. Proc.*, pp. 245–254, 1997.
[12] D.-P. Chen and H. A. Haus, "Analysis of metal-strip SAW gratings and transducers," *IEEE Trans. Sonics Ultrason.*, vol. SU-32, no. 3, pp. 395–408, 1985.
[13] H. A. Haus and W. Huang, "Coupled-mode theory," in *Proc. IEEE*, vol. 79, no. 10, pp. 1505–1518, 1991.
[14] V. P. Plessky, D. P. Chen, and C. S. Hartmann, "'Patch' improvements to COM model for leaky waves," in *IEEE Ultrason. Symp. Proc.*, pp. 297–300, 1994.
[15] K. Honkanen, J. Koskela, V. P. Plessky, and M. M. Salomaa, "Parasitic BAW excitation in LSAW transducers," in *IEEE Ultrason. Symp. Proc.*, pp. 949–952, 1998.
[16] V. P. Plessky, S. N. Kondratiev, and C. Lambert, "Reduced passband ladder type SAW impedance element filters on strong piezoelectric substrates," in *IEEE Ultrason. Symp. Proc.*, pp. 11–14, 1996.
[17] V. P. Plessky and C. S. Hartmann, "Characteristics of leaky SAWs on 36-$LiTaO_3$ in periodic structures of heavy electrodes," in *IEEE Ultrason. Symp. Proc.*, pp. 1239–1242, 1993.
[18] H. Yatsuda, "Modeling of parasitic effects for flip-chip SAW filters," in *IEEE Ultrason. Symp. Proc.*, pp. 143–146, 1997.
[19] S. Mineyoshi, O. Kawachi, M. Ueda, Y. Fujiwara, H. Furusato, and O. Ikata, "Analysis and optimal SAW ladder filter design including bonding wire and package impedance," in *IEEE Ultrason. Symp. Proc.*, pp. 175–178, 1997.
[20] J. V. Knuuttila, P. T. Tikka, C. S. Hartmann, V. P. Plessky, and M. M. Salomaa, "Anomalous asymmetric acoustic radiation in low-loss saw filters," *Electron. Lett.*, vol. 35, no. 13, pp. 1115–1116, 1999.
[21] J. V. Knuuttila, P. Tikka, V. P. Plessky, T. Thorvaldsson, and M. M. Salomaa, "Laser interferometric analysis of a ISM band SAW duplexer," in *IEEE MTTS Digest*, vol. 4, pp. 1449–1452, 1999.
[22] V. P. Plessky and S. N. Kondratiev, "Miniature SAW duplexer for ISM mobile phones," in *EFTF Proc.*, pp. 466–469, 1997.
[23] F. S. Hickernell, H. D. Knuth, R. C. Dablemont, and T. S. Hickernell, "The surface wave propagation characteristics of 64° Y-X $LiNbO_3$ and 36° Y-X $LiTaO_3$ substrates with thin-film $SiO_2$," in *IEEE Ultrason. Symp. Proc.*, pp. 345–348, 1995.
[24] G. Fischerauer, D. Gogl, R. Weigel, and P. Russer, "Investigation of parasitic effects in multi-transducer SAW RF filters," in *IEEE Ultrason. Symp. Proc.*, pp. 241–244, 1994.
[25] K. Nabors and J. White, "Multipole-accelerated capacitance extraction algorithms for 3-D structures with multiple dielectrics," *IEEE Trans. Circuits Syst.-I*, vol. 39, no. 11, pp. 946–954, 1992.
[26] ——, "Fastcap: A multipole accelerated 3-D capacitance extraction program," *IEEE Trans. Computer-Aided Design*, vol. 10, no. 11, pp. 1447–1459, 1991.
[27] C.-T. Tsai, "Package inductance characterization at high frequencies," *IEEE Trans. Comp. Packag., Manufact. Technol. B*, vol. 17, no. 2, pp. 175–181, 1994.
[28] D. K. Cheng, *Field and Wave Electromagnetics*, 2nd ed. Reading, MA: Addison-Wesley, 1989.
[29] M. Kamon, M. J. Tsuk, and J. K. White, "Fasthenry: A multipole-accelerated 3-D inductance extraction program," *IEEE Trans. Microwave Theory Tech.*, vol. 42, no. 9, pp. 1750–1758, 1994.
[30] H. A. Wheeler, "Formulas for the skin effect," in *Proc. IRE*, vol. 30, pp. 412–424, Sep. 1942.
[31] J. R. Carson, "Wave propagation over parallel wires: The proximity effect," *Phil. Mag.*, vol. 41, pp. 607–633, Apr. 1921.
[32] J. D. Cockcroft, "Skin effect in rectangular conductors at high frequencies," in *Proc. Royal Soc.*, vol. 122, pp. 533–542, 1929.
[33] T. Makkonen, "Modelling electromagnetic couplings in a SAW filter," M.S. Thesis, Dep. Technical Phys., Faculty of Information Technology, Helsinki University of Technology, Espoo, Finland, 1996.
[34] D. P. Morgan, *Surface-Wave Devices for Signal Processing*. Amsterdam: Elsevier, 1991.
[35] M. Valtonen, P. Heikkilä, H. Jokinen, and T. Veijola, "APLAC—object-oriented circuit simulator and design tool," in *Low-Power HF Microelectronics—A Unified Approach*. G. Machado, Ed. Lavenham, England: Lavenham Press Ltd., 1996.
[36] H. H. Ou, N. Inose, and N. Sakamoto, "Improvement of ladder-type saw filter characteristics by reduction of inter-stage mismatching loss," in *IEEE Ultrason. Symp. Proc.*, pp. 97–102, 1998.
[37] J. Knuuttila, P. Tikka, V. P. Plessky, T. Thorvaldsson, and M. M. Salomaa, "Recent advances in laser-interferometric investigations of SAW devices," in *IEEE Ultrason. Symp. Proc.*, pp. 161–164, 1997.
[38] J. V. Knuuttila, P. T. Tikka, and M. M. Salomaa, "Scanning michelson interferometer for imaging surface acoustic wave fields," *Optics Lett.*, vol. 25, no. 9, pp. 613–615, 2000.
[39] M. P. da Cunha, "High velocity pseudo surface wave (HVP-SAW): Further insight," in *IEEE Ultrason. Symp. Proc.*, pp. 97–106, 1996.
[40] S. Jen and C. S. Hartmann, "Laser probe investigation of leaky surface waves on 41° and 64°-$LiNbO_3$," in *IEEE Ultrason. Symp. Proc.*, pp. 293–296, 1994.
[41] J. Koskela, J. V. Knuuttila, T. Makkonen, V. P. Plessky, and M. M. Salomaa, "Acoustic loss mechanisms in leaky SAW resonators on lithium tantalate," *IEEE Trans. Ultrason., Ferroelect., Freq. Contr.*, accepted for publication.
[42] J. Koskela, J. V. Knuuttila, P. T. Tikka, C. S. Hartmann, V. P. Plessky, and M. M. Salomaa, "Mechanism for acoustic leakage in surface-acoustic wave resonators on rotated Y-cut lithium tantalate substrate," *Appl. Phys. Lett.*, vol. 75, no. 17, pp. 2683–2685, 1999.
[43] J. V. Knuuttila, J. Koskela, P. T. Tikka, C. S. Hartmann, V. P. Plessky, and M. M. Salomaa, "Asymmetric acoustic radiation in leaky SAW resonators on lithium tantalate," in *IEEE Ultrason. Symp. Proc.*, pp. 83–86, 1999.

**Tapani Makkonen** (M'98) was born in Helsinki, Finland in 1968. He received the M.Sc. degree in engineering physics from the Helsinki University of Technology in June 1996 after which he joined the Materials Physics Laboratory as a Ph.D. student. His research interests include modeling of package parasitic effects in SAW devices, and, currently, he is focusing on the FEM modeling of thin-film bulk-acoustic wave resonators. Mr. Makkonen is a member of the Finnish Physical Society.

**Serguei N. Kondratiev** received the B.S., M.S., and Ph.D. degrees in physics and mathematics from the MPTI (Moscow) in 1969, 1972, and 1976, respectively. He also received the D.Sc. degree in 1992. He worked at Mints Radiotechnical Institute Russian Academy of Science from 1972 to 1980 as Senior Scientist. In 1980, he joined the Scientific Research Institute "Phonon," where he worked as SAW Filter Division Chief. Since 1993, he has been employed as Principal Research Engineer at Advanced SAW Products and Micronas Semiconductors, Switzerland. He currently is Principal Designer at Temex SAW. In 1993, he was awarded the Russian State Price for creating the scientific basis for developing and introducing SAW into radioelectronics in Russia. Dr. Kondratiev has authored and co-authored more than 100 patents and patent applications. He is a member of IEEE Ultrasonics, Ferroelectronics, and Frequency Control Society. His research interests are in area of physics and design and modelling of SAW devices.

**Victor P. Plessky** (M'93) received his Ph.D. degree in the physical and mathematical sciences at the Moscow Physical-Technical Institute and the Dr.Sc. degree at the Institute of Radio Engineering and Electronics (IRE, Russian Academy of Sciences, Moscow) in 1978 and 1987, respectively. Beginning in 1978, he worked at IRE, first as Junior Researcher and, in 1987, was promoted to Laboratory Director. In 1991, he also worked as a professor at the Patris Lumumba University, Moscow. He received the title of Full Professor in 1995 from the Russian Government. In 1992, he joined ASCOM Microsystems SA, in Bevaix, Switzerland, where he worked as special SAW projects manager. He was a visiting professor at the Helsinki University of Technology in April and May 1997. Since 1998, he has been working at Thomson Microsonics. He has been engaged in research on semiconductor physics, SAW physics (new types of waves, scattering and reflection on surface irregularities, laser generation of SAW), SAW device development (filters, delay lines, RACs), and magnetostatic wave studies. Currently, his interests focus on SAW physics and low-loss SAW filter development. Prof. Plessky is an IEEE member. He was awarded the USSR National Award for Young Scientists in 1984.

**Thor Thorvaldsson** (S'81–M'82–S'82–M'86–S'87–M'87) was born in Reykjavik, Iceland on October 14, 1953. He received the electrical engineering degree from the University of Iceland in 1977 and the degree of Doctor of Technical Sciences from the Swiss Federal Institute of Technology (ETH) in Zürich, Switzerland in 1988. He was with the ETH Laboratory of Electromagnetic Fields and Microwave Electronics, Zürich from 1977 to 1979 as a graduate student in the field of telecommunications and after 1979 as a research associate engaged in teaching as well as research of microwave and SAW devices.

He has held the positions of Visiting Scientist at Siemens SAW-Group, Munich, Germany; Visiting Scholar at University of São Paulo, Brazil; and a Post-Doctorate Research Associate at the University of Central Florida, USA, where he did research on unidirectional SAW transducers. After returning from the USA in 1989, he became the group leader of the SAW group at ETH, where he worked on software development for modeling of SAW devices. He joined Advanced SAW Products SA in Bevaix, Switzerland in 1992 as Senior Engineer and became the R&D manager of the SAW group at Micronas Semiconductor SA in 1996. In 1998, he founded the SAW consulting company Thoronics GmbH in Bevaix, Switzerland. His area of concentration is surface wave propagation phenomena, modelling of low loss SAW filters, and development of design techniques.

**Julius Koskela** (M'98) received the M.Sc. degree in technical physics from Helsinki University of Technology (HUT) in 1996. He obtained the DrTech degree in January 2001 in the Materials Physics Laboratory at HUT. His research interests include SAW physics and modeling SAW devices. He is a member of the Finnish Physical Society.

**Jouni V. Knuuttila** received the M.Sc. degree in technical physics from Helsinki University of technology (HUT) in 1998. He is a postgraduate student in the Materials Physics Laboratory at HUT. His research interests include optical imaging of surface and bulk acoustic waves, sonoluminescence, and audio signal processing. He is a member of the Finnish Optical Society.

**Martti M. Salomaa** received his DrTech degree in technical physics from Helsinki University of Technology (HUT) in 1979. Thereafter, he worked at UCLA and the University of Virginia. From 1982 to 1991, he was the theory group leader at the Low Temperature Laboratory, HUT, and from 1988 to 1991, he served as the director of the ROTA project between the Academy of Finland and the Soviet Academy of Sciences. He has held a sabbatical stipend at the University of Karlsruhe, and, in 1994, he was a guest professor at ETH-Zürich. Since 1996, he has been a professor of technical physics and the Director of the Materials Physics Laboratory in the Department of Technical Physics and Mathematics at HUT. He is a co-recipient of the 1987 Award for the Advancement of European Science (presented by the Körber Foundation, Hamburg). His research interests include superfluidity, superconductivity, magnetism, physics of SAW, nondiffracting waves, and mesoscopic physics. He is a member of the IEEE, APS, EPS, and the Finnish Physical and Optical Societies.